

VIP Very Important Paper

www.batteries-supercaps.org

Texturing (002)-Oriented Zinc Atop a Cotton Cloth for High-Performance Zn-Ion Batteries

Napat Kiatwisarnkij,^[a, b] Zehao Song,^[b] Chanin Tangpongkitjaroen,^[a] Suttipong Wannapaiboon,^[c] Xinyu Zhang,^[d] Panyawat Wangyao,^[a] and Jiaqian Qin^{*[b]}

Zn-ion batteries emerge as a promising alternative to conventional Li-ion batteries due to their superior environmental friendliness and high safety, making them suitable for sustainable energy storage in various applications. However, concerns persist regarding the limitations of Zn-ion batteries, such as uncontrolled dendrite growth and side reactions. In this study, the electroplating method was employed to deposit (002) plane-dominated textures on a modified cotton cloth substrate, which consists of a silver conductive layer atop a cotton supporting layer. The electroplating current density and time are critical for the fabrication of dense and compact (002) Zn textures. The optimized condition for this process involves a

current density of 40 mA/cm² and an electroplating time of 30 minutes. Compared to (101)-dominated Zn anodes, the (002)-dominated electrode demonstrates faster deposition kinetics and lower charge transfer resistance, enabling denser and more uniform Zn deposition. Additionally, the (002)-dominated electrode also exhibits an enhanced ability to inhibit side reactions in the mild aqueous electrolyte, further improving the lifespan of Zn-ion batteries. This work demonstrates the feasibility of using ordinary cotton cloth as a substrate for electroplating (002)-dominated Zn, thereby expanding the potential applications of Zn-ion batteries.

1. Introduction

Zinc-ion batteries (ZIBs) are emerging as a promising alternative to lithium-ion batteries (LIBs) due to the abundant availability of Zn sources on Earth, environmental sustainability, higher safety, and a simpler manufacturing process.^[1] Moreover, ZIBs exhibit a high theoretical capacity of 820 mA·h/g and a low corrosion potential of -0.76 V vs. the standard hydrogen electrode. However, ZIBs face limitations, including uncontrollable Zn dendrite growth and hydrogen evolution reactions (HER).^[2] The crystalline structure of zinc (Zn) metal is hexagonal close-packed, fundamentally exhibiting high anisotropy in electro-crystallization, leading to chaotic dendrite growth during the charging/discharging process. These dendrites can cause swelling and short-circuit issues in the battery, resulting in reduced lifespan.^[3] Since the reduction potential of metal Zn is higher than the standard hydrogen electrode, parasitic hydrogen evolution reactions typically accompany Zn deposi-

tion during the plating process. In aqueous ZIBs, hydrogen evolution reactions can alter the local pH, generating undesired by-products (e.g., zinc oxides or hydroxides), which weaken the reversibility between Zn and Zn²⁺.^[2,4]

In recent years, numerous strategies have been employed to address these challenges, with efforts focusing on surface modification and structural design of anodes,^[1a,c,4c,5] separator improvements,^[6] and electrolyte optimization.^[7] Among these solutions, constructing (002)-oriented Zn anodes is considered a fundamental and promising strategy to simultaneously suppress dendrite growth and HER.^[8] Zn (002) planes exhibit higher corrosion resistance than Zn (101) and (100) planes in sulfate-based electrolytes, owing to the higher activation energy for Zn dissolution.^[9] In principle, Zn deposition is favorable on (101) and (002) orientations in the mild electrolyte of 2 M ZnSO₄, as (100) planes have higher surface energy than (101) and (002) planes. However, the morphologies of these planes differ: the (101) and (002) planes orient in the declined and horizontal directions with respect to the substrate, respectively. The top of the declined (101) planes can alter the local electric field, worsening Zn deposition behavior in subsequent charging/discharging cycles, referred to as the “tip” effect. This effect would prompt the accumulation of Zn on the top of the (101)-plane-dominated grain, leading to the formation of extremely large dendrites.^[8b] The dendrites may pierce the separator and attach to the cathode, causing short-circuiting and limiting the lifespan of ZIBs. In contrast, the (002) planes are parallel to the substrate, maintaining a uniform electric field and alleviating the tip effect. Note that the majority of commercial Zn foils are (101)-dominated. Therefore, constructing (002)-dominated Zn electrodes is crucial for high-performance ZIBs with more stable anodes.

[a] N. Kiatwisarnkij, C. Tangpongkitjaroen, P. Wangyao
Department of Metallurgical Engineering, Faculty of Engineering, Chulalongkorn University, Bangkok 10330, Thailand

[b] N. Kiatwisarnkij, Z. Song, J. Qin
Center of Excellence in Responsive Wearable Materials, Department of Materials Science, Faculty of Science, Chulalongkorn University, Bangkok 10330,
E-mail: jiaqian.q@chula.ac.th

[c] S. Wannapaiboon
Synchrotron Light Research Institute (Public Organization), Nakhon Ratchasima 30000, Thailand

[d] X. Zhang
State Key Laboratory of Metastable Materials Science and Technology, Yanshan University, Qinhuangdao, 066004 P. R. China

 Supporting information for this article is available on the WWW under <https://doi.org/10.1002/batt.202400727>

Compared to other complex metallic crystallization methods (e.g., zone melting^[10] or Bridgman methods),^[10–11] electroplating offers several advantages, including easier accessibility, a more convenient operation process, lower energy consumption, and good tolerance to substrate size variations.^[12] Controlling electroplating current and time is a common and effective method for modifying the crystal structures of electroplated metals, widely used in metallic texture fabrication, such as (111)-oriented Au films^[13] or eutectic ZnAl alloys.^[14] Herein, we investigate the impact of electroplating current density and time on Zn crystalline structures atop a modified cotton cloth substrate. To promote the commercial application of ZIBs, we chose economical cotton cloth rather than expensive textured

metal foils (e.g., (002)-oriented Zn foil^[8b] or (100)-faceted Cu substrate).^[15] Additionally, cotton cloth-based ZIBs may have promising potential for wearable device applications. Consequently, anodes fabricated at an electroplating current density of $J_{EP}=40 \text{ mA/cm}^2$ for 30 minutes exhibit dense and uniform (002)-oriented Zn textures, resulting in enhanced stability in symmetric batteries and Zn||MnO₂ full batteries.

2. Results and Discussion

Figure 1a illustrates the fabrication process of modified Zn anodes, including the blade coating of silver (Ag) powder onto

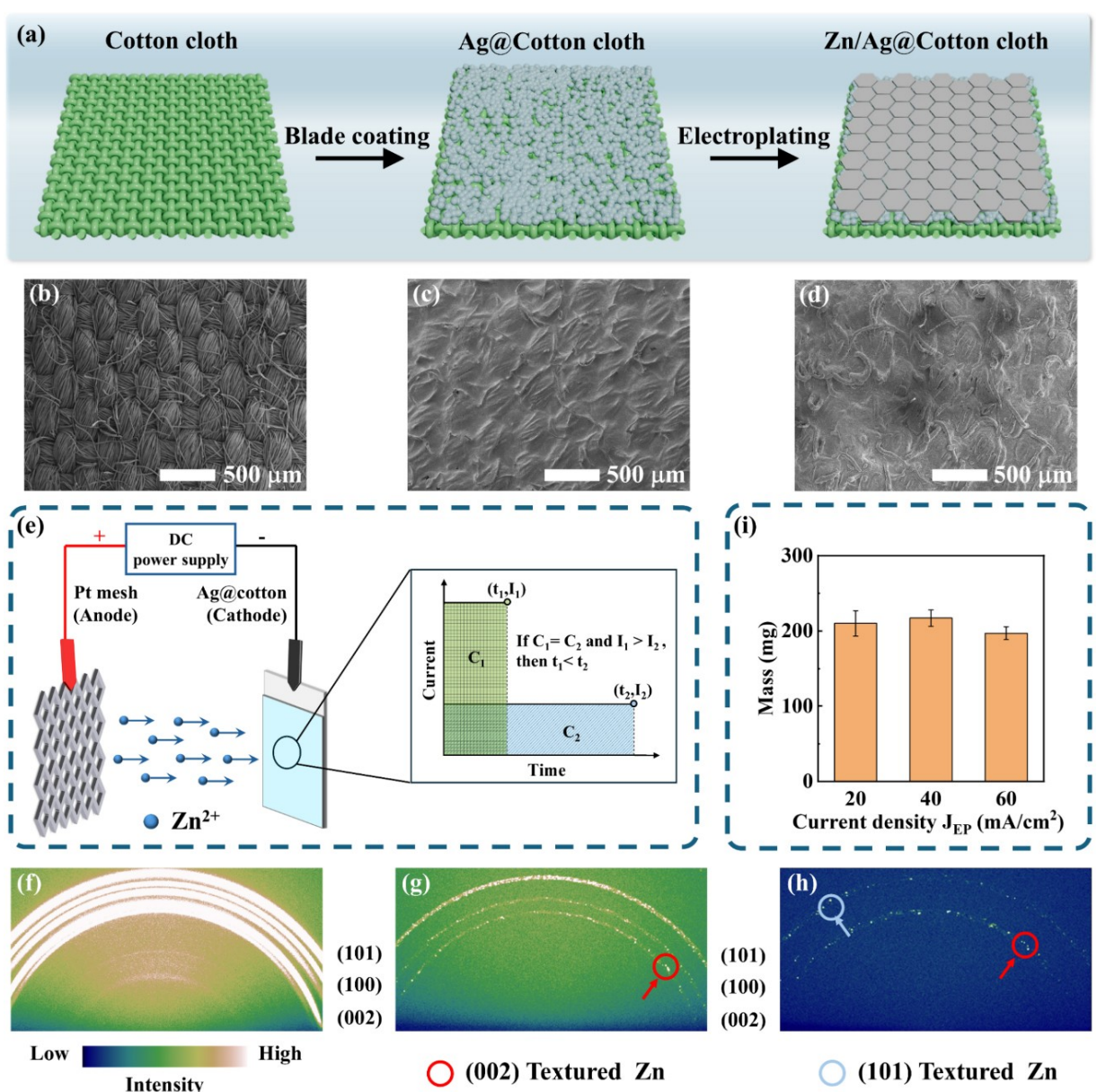


Figure 1. (a) Fabrication diagram of Zn/Ag@cotton cloth. SEM images depicting the surface morphology of cotton cloth (b), Ag@cotton cloth (c), and Zn/Ag@cotton cloth (d). (e) The working principle of the electroplating system. The inset figure explains the relationship between electroplating time t and current I under the same capacity C . (f–h) GI-XRD analysis of the electroplated Zn at different electroplating times with a current density of $J_{EP}=40 \text{ mA/cm}^2$. (i) The mass of the Zn layer at different electroplating current densities J_{EP} for a capacity of $20 \text{ mA}\cdot\text{h}/\text{cm}^2$.

a cotton cloth and subsequent electroplating deposition of (002)-oriented Zn textures. The addition of a silver conductive layer onto the cotton cloth substrate is critical for the electroplating of Zn, as the electroplating process requires a conductive substrate to create an electrical pathway, allowing ions in the electrolyte to reach the substrate (Figure S1). Silver has good electrical conductivity and high affinity with Zn metal, making it a conductive material in this case. Compared to other metals like copper and tin, silver exhibits superior oxidation resistance, minimizing the reduction of electroplating efficiency caused by native oxides on the metal surface.^[16] The diameter of the Ag powders used in this case is approximately 1~3 µm (Figure S2), facilitating effective gap filling within the cotton cloth substrate, creating a relatively flat and even surface for Zn electroplating, as observed by scanning electron microscopy (SEM). Compared to the curved surface of the cotton cloth, the relatively flat surface of Ag@cotton cloth is advantageous for electroplating a (002)-oriented Zn layer (Figures 1b and 1c). The curved surface may cause Zn grains to compress against each other, leading to crystal growth in undesired orientations due to uneven strain distribution. In contrast, a flat surface with uniform strain distribution encourages more controlled and even growth of the (002)-oriented Zn layer.^[17] Besides creating a conductive electrode for electroplating, the silver layer can also enhance the flatness of the cotton cloth-based substrate,^[18] enabling the uniform electroplating of the (002)-oriented Zn layer.^[19] Furthermore, their alloy Ag_xZn_y features high electrochemical stability in mild aqueous electrolytes and excellent mechanical tolerance to deformation.^[20] Figure 1d demonstrates the surface morphology of Zn/Ag@cotton cloth after electroplating. Compared to Ag@cotton cloth, the electroplated Zn fills the empty spaces inside the cotton fibers, resulting in a smoother surface for the Zn/Ag@cotton cloth anode. This even surface of the electroplated anode alleviates the disordered electric field distribution, suppressing Zn dendrite growth and contributing to high-performance Zn-ion batteries.

Figure 1e depicts the mechanism of the Zn electroplating process. A direct current (DC) power source supplies a constant current to the electroplating system, where the Ag@cotton cloth substrate and a platinum mesh are connected to the negative and positive electrodes of the DC power source, respectively. In the electrolyte, Zn²⁺ ions are driven by an electric field to migrate toward the Ag@cotton cloth electrode, where they are reduced to Zn metal and deposited on the electrode surface by receiving electrons from the external circuit. The mass of electroplated Zn on the Ag@cotton cloth highly depends on the electroplating current and time, as described by the following equation:^[12,21]

$$m = \int_0^t \frac{A_w \cdot I}{z \cdot F} dt \approx \frac{A_w \cdot I \cdot t}{z \cdot F} \quad (1)$$

where m is the electroplated Zn mass on the cathode surface, A_w is the atomic mass of Zn, I is the electroplating current, t is the electroplating time, z is the valence number of ions (2 for Zn²⁺), and F is the Faraday constant. This equation suggests that the electroplated Zn mass is approximately proportional to

both the electroplating current and time at a constant electroplating current. In this work, we kept the Zn mass constant at different electroplating current densities J_{EP} to mitigate the impact of Zn thickness on battery performance. Therefore, a larger electroplating current density corresponds to a shorter electroplating time to maintain the same mass at different current densities.

2D grazing incidence X-ray diffraction (GIXRD) characterization was conducted to investigate the crystalline structures of the Zn/Ag@cotton cloth electrodes, fabricated at different electroplating times, with a constant electroplating current density of $J_{EP}=40\text{ mA/cm}^2$. The sharp diffraction rings in Figure 1f reveal that the Zn layer electroplated after 1 minute is polycrystalline, with (002), (100), and (101) planes. The ring beneath the Zn (100) peak originates from the Zn–Ag alloy. Furthermore, the deformation of the Zn (002) ring is attributed to the lattice mismatch between the Ag–Zn compound and the electroplated Zn.^[22] When the electroplating time increases to 30 minutes, the grains of polycrystalline Zn continue to grow, resulting in Zn textures (as indicated by the red circle in Figure 1g). Due to the increased thickness of the electroplated Zn layer, the Zn–Ag alloy and its related distortion disappear. Extending the electroplating time further to 60 minutes reveals both (002) and (101) textures, as depicted in Figure 1h. Therefore, the optimal electroplating time is 30 minutes at the current density of 40 mA/cm² to achieve (002)-dominated Zn electrodes. In contrast, excessive electroplating time leads to the exposure of (101) planes, causing the electroplated Zn layer to shift from (002)- to (101)-dominated Zn (Figure S3).

According to Equation 1, if the mass remains constant, electroplating times for current densities of $J_{EP}=20$ and 60 mA/cm^2 should be 60 and 20 minutes, respectively. Figure 1i shows that three electroplated Zn electrodes, each measuring 3.5×3.5 cm², exhibit comparable masses ranging from 197.0 to 217.0 mg, corresponding to thicknesses ranging from 22.5 to 24.8 µm (the mass density applied here is 7.14 g/cm³).

Figure 2a illustrates the Zn nucleation and crystal growth under different electroplating current densities. The electroplating current density (J_{EP}) can adjust the nucleation rate (N_c) in the crystal nucleation and growth process, which is given by:^[2d,23]

$$N_c \propto \exp\left(-\frac{1}{\log^2 J_{EP}}\right) \quad (2)$$

Therefore, a larger current density J_{EP} corresponds to a higher nucleation rate, resulting in a denser nucleus distribution, as shown in Figure 2a. At a low current density (upper panels in Figure 2a), only a few nuclei form on the substrate, leading to excessive gaps and sparse distribution. During the subsequent crystal growth stage, these large gaps allow Zn islands to grow independently without attaching to neighboring grains, resulting in the exposure of (101) planes and the formation of truncated hexagonal pyramid-like grains in the ZnSO₄ electrolyte (Figure S3d). Increasing the current density to an appropriate value enhances the nucleation rate, establishing proper spacing between adjacent nuclei, which results in a

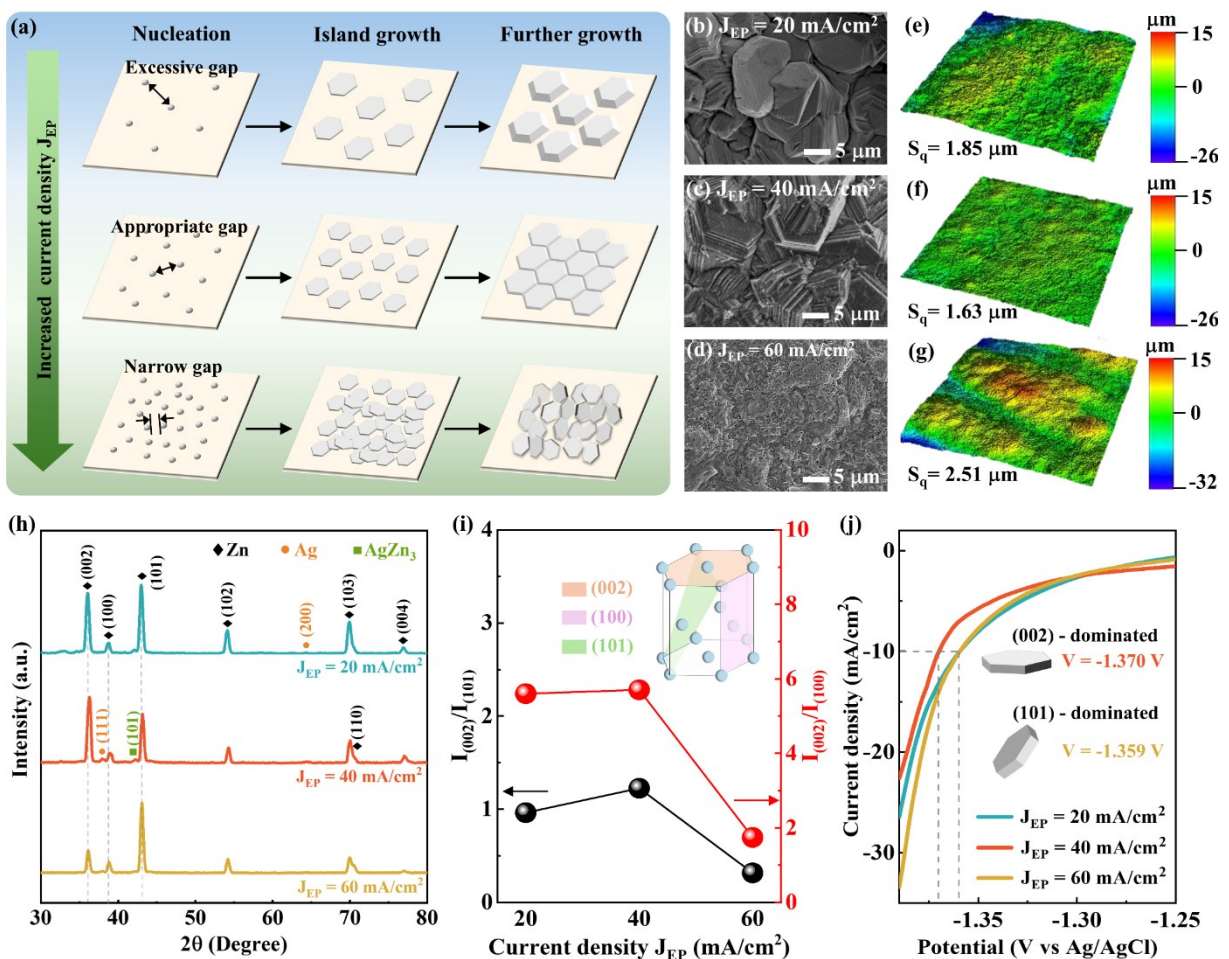


Figure 2. (a) Zn nucleation and crystal growth at different electroplating current densities J_{EP} . (b-d) SEM images of Zn/Ag@cotton cloth electrodes electroplated at different current densities. (e-g) Surface roughness of these electrodes fabricated at various current densities. (h) XRD pattern of different Zn/Ag@cotton cloth electrodes. (i) The impact of electroplating current density on Zn crystal structure. The ratios $I_{(002)}/I_{(101)}$ and $I_{(002)}/I_{(100)}$ are calculated from panel (h). The inset figure illustrates the schematic of different crystalline planes. (j) LSV curves of different electrodes in a $1 \text{ M Na}_2\text{SO}_4$ electrolyte.

compact (002)-oriented Zn layer that effectively covers the substrate surface. However, controlling the electroplating time is also crucial for achieving a (002)-oriented Zn layer, as excessive time can reveal (101) planes again. For instance, X-ray diffraction (XRD) analysis can demonstrate a transition from (002)-to (101)-dominated Zn with extended electroplating time at $J_{EP} = 40 \text{ mA}/\text{cm}^2$. Additionally, excessively high electroplating current densities can result in an abundance of nuclei with limited spacing, causing overlap of Zn grains and leading to lattice mismatch or stress at the overlapped interfaces, which can further promote crystal growth along other orientations.^[9,24]

Figures 2b, 2c, and 2d show SEM images of the electroplated Zn layer at current densities of $J_{EP} = 20$, 40 , and $60 \text{ mA}/\text{cm}^2$ respectively. The best electroplating current density is $J_{EP} = 40 \text{ mA}/\text{cm}^2$ in this case. At an extremely low electroplating current density of $J_{EP} = 10 \text{ mA}/\text{cm}^2$, a mixture of mossy-like microstructures and plate-shaped grains appears on the surface of the electroplated electrode (Figure S4a). Moreover, Zn electroplated at an excessive current density of $J_{EP} = 80 \text{ mA}/\text{cm}^2$ exhibits a dendrite-like surface (Figure S4b). The areal surface roughness of electroplated Zn at $J_{EP} = 20$, 40 , and $60 \text{ mA}/\text{cm}^2$ is

shown in Figures 2e–2g. The surface roughness of Zn electroplated at $J_{EP} = 20$ and $40 \text{ mA}/\text{cm}^2$ is similar, due to the uniform and dense Zn alignment. Conversely, Zn electroplated at $J_{EP} = 60 \text{ mA}/\text{cm}^2$ has higher surface roughness because excessive Zn nucleation at the initial stage accelerates non-compact Zn growth (Figure 2a).

In Figure 2h, all three electrodes exhibit the major peaks of Zn metal (PDF: 04-0831), including the (002), (100), (101), (102), (103), (110), and (004) planes. The electrode made at $J_{EP} = 40 \text{ mA}/\text{cm}^2$ demonstrates a (002)-dominated crystal orientation with a relative texture coefficient of 37.7% (Figure S5), while the other electrodes are mainly filled with (101)-oriented Zn grains. Some peaks related to Ag metal (PDF: 04-0783) and AgZn₃ alloy (PDF: 25-1325) also appear in the XRD patterns. Figure 2i shows the calculated intensity ratios of peaks $I_{(002)}/I_{(101)}$ and $I_{(002)}/I_{(100)}$ for these Zn/Ag@cotton cloth electrodes. The electrode fabricated at $J_{EP} = 40 \text{ mA}/\text{cm}^2$ exhibits the highest ratio of $I_{(002)}/I_{(101)}$ and $I_{(002)}/I_{(100)}$, confirming that it is (002)-plane dominated, while the others are primarily oriented along the (101) planes (Figure 2h).

Figure 2j depicts linear sweep voltammetry (LSV) curves of different electrodes in a 1 M Na₂SO₄ electrolyte. The anode electroplated at $J_{EP}=40 \text{ mA/cm}^2$ exhibits a lower voltage (-1.370 V) than the others, indicating that the (002)-dominated Zn exhibits stronger suppression of HER than the (101)-oriented ones. This result aligns with other reports.^[8e,25] Jingmin Zhang et al. compared the change in Gibbs free energy after H was adsorbed on different Zn planes through theoretical calculations. Their results demonstrated that (002) planes require more activation energy for HER compared to (101) facets.^[8e] Additionally, Miao Zhou et al. compared the free energy of hydrogen adsorption between (100) and (002) planes. They found that (002)-dominated Zn required higher free energy for hydrogen adsorption than the (100)-faceted one, leading to HER suppression.^[25a] Moreover, their theoretical simulations implied that (002) planes form stronger chemical bonds to suppress Zn dissolution. Tafel curves in Figure S6 indicate higher corrosion resistance of the (002) plane as well. Figure S7 shows that the (002)-dominated Zn electrode has a smaller contact angle than the (101)-dominated one when exposed to a droplet of 2 M ZnSO₄ electrolyte.

To characterize the long-term stability of the Zn/Ag@cotton cloth electrodes, we assembled symmetric batteries paired with a 2 M ZnSO₄ electrolyte and a glass fiber separator. Figure 3a depicts the rate performance of these Zn/Ag@cotton cloth electrodes in Zn||Zn symmetric batteries at different current densities and a constant areal capacity of 1 mA·h/cm². The electrode fabricated at $J_{EP}=40 \text{ mA/cm}^2$ delivers the lowest overpotential hysteresis at all applied current densities. Furthermore, Figure 3b plots the overpotentials as a function of current density, where the slope characterizes the deposition kinetics of Zn²⁺ ions. The relationship between overpotential hysteresis (η_{tot}) and the applied current density (i) follows:

$$i = i_0 \frac{F \eta_{tot}}{RT z} \quad (3)$$

where i_0 is the exchange current density, F is the Faraday constant, R is the gas constant, and T is the temperature. The variable z represents the number of electrons participating in the electrode reaction, with $z=2$ for Zn-ion batteries. Similarly, the anode electroplated at $J_{EP}=40 \text{ mA/cm}^2$ shows the largest exchange current density of $i_0=2.58 \text{ mA/cm}^2$, corresponding to the fastest deposition kinetics. Therefore, the (002) plane-dominated electrode induces faster deposition kinetics than the (101)-dominated one. This may result from the smaller surface roughness of the compact (002)-oriented Zn layer.^[26] Faster deposition kinetics can promote the formation of a larger critical nucleation radius, subsequently enabling more compact Zn deposition and thus suppressing dendrite growth.^[22] Additionally, the CV curves of asymmetric batteries in Figure S8 suggest a lower nucleation overpotential for the (002)-dominated electrode, further supporting this argument regarding nucleation.

Figure 3c illustrates the stability of these anodes at an applied current density of 1 mA/cm² and an areal capacity of 0.5 mA·h/cm². The overpotential hysteresis of the three electro-

des fabricated at electroplating current densities of $J_{EP}=20, 40$, and 60 mA/cm^2 are 213.9, 202.9, and 300.1 mV, respectively (see the inset figure of Figure 3c). Therefore, the (002)-dominated electrode exhibits the lowest overpotential hysteresis, in agreement with the rate-performance results in Figure 3a. The electrode prepared at the electroplating current density of $J_{EP}=40 \text{ mA/cm}^2$ demonstrates the longest lifetime of more than 700 hours. Thus, the (002)-oriented electrode enables a longer lifespan than the (101)-dominated one. Similarly, at higher current densities of 5 mA/cm² (areal capacity of 2.5 mA·h/cm²) and 10 mA/cm² (areal capacity of 5 mA·h/cm²), Zn electroplated at $J_{EP}=40 \text{ mA/cm}^2$ also shows better stability than the others (Figure S9). The extended lifespan is likely due to the synergistic contribution of multiple factors, including mitigated dendrite growth and suppressed hydrogen evolution reactions.

The electrochemical impedance spectroscopy (EIS) of symmetric batteries indicates that the charge transfer resistances of electrodes fabricated at electroplating current densities of 20, 40, and 60 mA/cm^2 are 142.5, 81.7, and 123.3Ω , respectively. (Figure 3d). Therefore, the (002)-dominated electrode exhibits a lower charge transfer resistance, corresponding to an easier transfer process of Zn²⁺ ions from the electrolyte to the anode surface.

Figure 3e shows the coulombic efficiency of these electrodes measured in asymmetric Zn||Cu batteries at a current density of 1 mA/cm² and an areal capacity of 0.5 mA·h/cm². All three electrodes exhibit nearly perfect coulombic efficiency of approximately 100%. However, the anode electroplated at $J_{EP}=40 \text{ mA/cm}^2$ demonstrates the best stability, with the longest lifespan of more than 300 cycles. Figure 3f shows the corresponding galvanostatic charge-discharge (GCD) curves of the electrode electroplated at $J_{EP}=40 \text{ mA/cm}^2$ over multiple cycles. The GCD curve profiles remain almost the same with an increased overpotential hysteresis. Figure 3g compares the GCD curves of the electrode fabricated at $J_{EP}=60 \text{ mA/cm}^2$. A distinct profile change appears at the 100th cycle, accompanied by a more significant growth of overpotential hysteresis. Therefore, this measurement confirms that the stability and reversibility of (002)-oriented Zn are superior to those of the (101)-dominated ones.

Figures 3h–3j illustrate the surface morphologies of various electrodes after 300 cycles in symmetric batteries tested at a current density of 1 mA/cm² and an areal capacity of 0.5 mA·h/cm². Compared to the other two electrodes, the anode fabricated under the current density of $J_{EP}=40 \text{ mA/cm}^2$ exhibits a more uniform surface morphology. In contrast to the (101)-dominated one, the (002)-dominated electrode maintains a flat surface after a few cycles, preventing immediate dendrite growth, which results in a longer lifespan. The XRD analysis in Figure S10 indicates that all three electrodes are dominated by the (101) orientation after cycling. It is expected that the (002)-dominated electrode would transition to the (101)-dominated one after cycling because, during the cyclic test, the (002)-dominated electrode undergoes continuous Zn plating/stripping, making it difficult to provide a stable and ideal environment for crystal growth. Additionally, the AgZn₃ alloy still exists in all samples, particularly in the anode electroplated at current

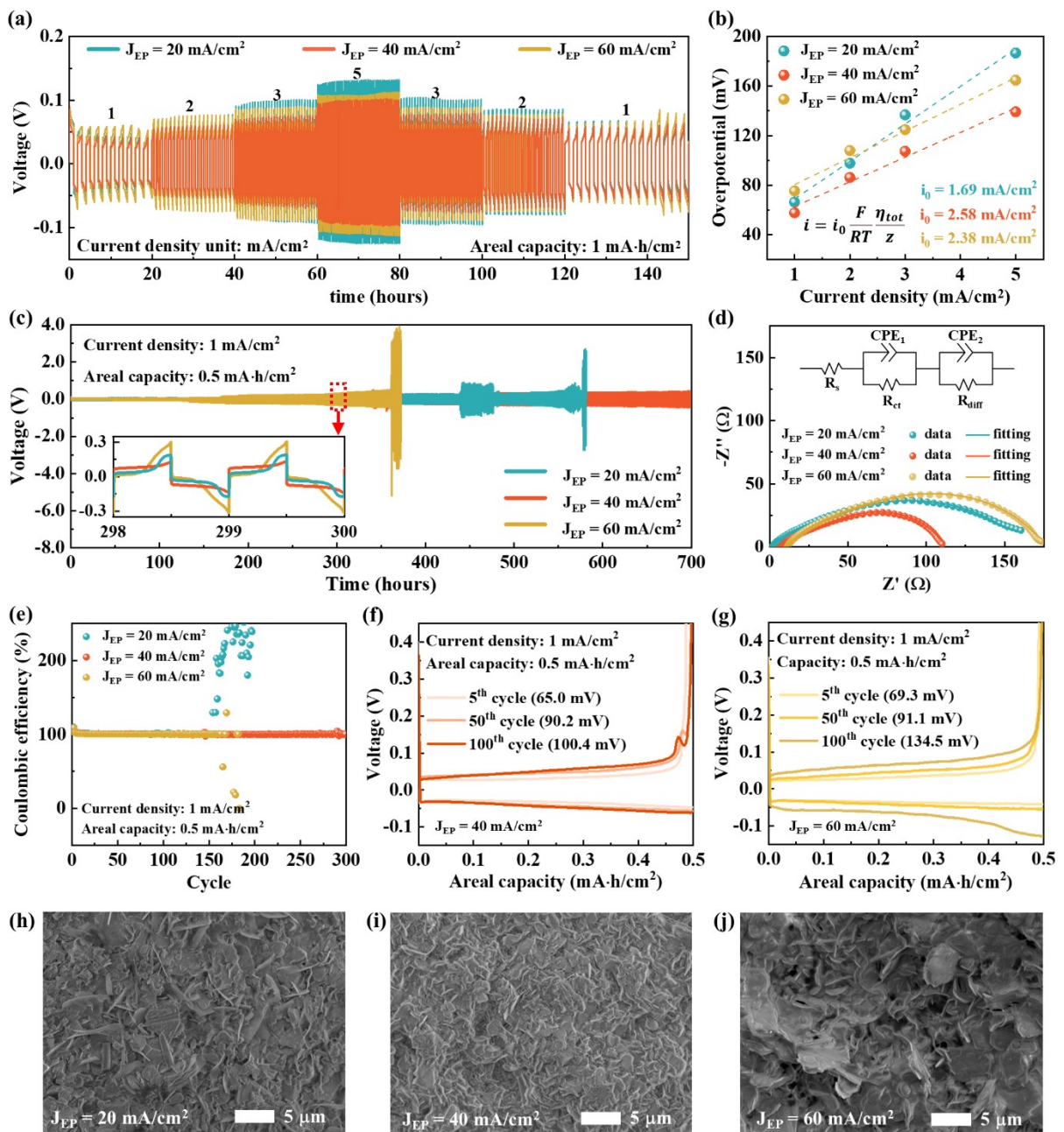


Figure 3. (a) Rate performance of three electrodes in symmetric batteries at various current densities and an areal capacity of 1 mA·h/cm². (b) Overpotential hysteresis as a function of electroplating current density. The exchange current density, i_0 , is determined by linearly fitting the slope. (c) Stability of different electrodes at a current density of 1 mA/cm² and an areal capacity of 0.5 mA·h/cm². The inset figure illustrates the detailed changes in voltage from cycles of 298 to 300. (d) EIS curves of various electrodes at the initial state. The inset figure depicts the equivalent circuit model. (e) Coulombic efficiency of Zn||Cu asymmetric batteries paired with different electrodes. The current density and areal capacity are 1 mA/cm² and 0.5 mA·h/cm², respectively. (f, g) GCD curves of three electrodes in asymmetric batteries measured after 5, 50, and 100 cycles. (h–j) Surface morphology of various anodes after cycling for 300 cycles. The current density and areal capacity are 1 mA/cm² and 0.5 mA·h/cm² respectively.

densities of 20 and 60 mA/cm². Zinc sulfate hydroxide by-products, such as $\text{Zn}_4\text{SO}_4(\text{OH})_6 \cdot 3\text{H}_2\text{O}$ (PDF: 39-0689) and $\text{Zn}_4\text{SO}_4(\text{OH})_6 \cdot 4\text{H}_2\text{O}$ (PDF: 44-0673), also appear in the XRD patterns. However, the anode electroplated at $J_{\text{EP}}=40$ mA/cm² demonstrates a lower peak intensity for these by-products compared to the others. Thus, the (002)-dominated electrode can suppress the generation of by-products. Normally, the insoluble and loose by-products can exacerbate chaotic den-

drite growth, as they lead to an uneven anode surface through continuous corrosion and passivation. The rough surface alters the local electric field distribution, prompting the formation of the “tip” effect, which results in larger dendrites. Moreover, because of their insoluble nature, the anode coated with by-products would waste more water and salt from the electrolyte, further shortening the lifespan of Zn-ion batteries.

Figure 4 illustrates the different Zn deposition behaviors on the (002)- and (101)-dominated anodes during cycling. With respect to the (101)-dominated anode, fresh Zn micro-sheets preferentially grow at the top region of the previous micro-structures, forming large, chaotic dendrites due to the tip effect. These dendrites increase the surface-to-volume ratio of the anode, thereby enhancing H₂ gas generation. In subsequent cycles, the hydrogen evolution reaction alters the pH value in the local region to alkaline, promoting the generation of insoluble by-products. As mentioned earlier, these by-products accelerate dendrite formation, leading to an irreversible “death spiral” that causes uncontrolled dendrite growth, ultimately resulting in degradation or short-circuiting issues.

In contrast, the (002) plane-dominated electrode is expected to allow epitaxial Zn growth, maintaining the uniformity of the substrate texture.^[24–25] The compact and even Zn epitaxial layer prevents the rapid formation of a death spiral, thereby enabling a longer lifespan for Zn-ion batteries. Furthermore, the (002)-dominated electrode effectively suppresses hydrogen evolution reactions and by-product generation, further reducing the likelihood of initiating a death spiral. Therefore, the (002)-plane dominated electrode is more stable than the (101)-dominated one during long-term battery testing.

The rechargeable full-battery configuration with a Zn anode, a glass fiber separator, and a γ -phase manganese dioxide (MnO_2) cathode in a 2 M ZnSO_4 electrolyte was also created to demonstrate practical applications (Figure 5a). $\gamma\text{-MnO}_2$ features an intergrowth phase that combines both β -phase and R-phase, accompanied by abundant tunnel channels for ion insertion^[27]

(see SEM and XRD analysis of MnO_2 in Figure S11). During discharge, Zn is stripped from the anode, and Zn^{2+} ions are inserted into the tunnels of $\gamma\text{-MnO}_2$.^[27] In principle, hydrogen ions (H^+) can also be inserted into MnO_2 , playing a crucial role in the electrochemical reactions of the MnO_2 cathode. These H^+ ions are believed to originate from the dissociation of free water molecules in the aqueous electrolyte. The N/P ratio of the full batteries with different anodes was calculated to compare the balance of energy density and cycle performance. The N/P ratio results show no significant difference across the different anodes, as indicated in Tables S1 and S2, due to the similar Zn mass and thickness of the anodes. Thus, the specific capacity and stability of the full batteries depend on the Zn micro-structure. Figure 5b shows cyclic voltammetry (CV) curves of different full batteries at a scan rate of 0.1 mV/s. All three CV curves display one redox peak at approximately 1.61 V, corresponding to the extraction reaction of Zn ions from the MnO_2 structure. Two reduction peaks, located at 1.35 and 1.14 V, correspond to the insertion of H^+ and Zn^{2+} ions into the MnO_2 cathode, respectively. Compared to the (101)-dominated anode, the (002)-oriented electrode generates a larger enclosed area in the CV curves. This suggests that the full battery paired with the (002)-oriented electrode can achieve higher specific capacity. This result aligns with the faster Zn deposition kinetics of the (002)-oriented electrode, as previously demonstrated. Nyquist plotting of different full batteries (Figure S12) suggests that the (002)-dominated anode exhibits a smaller charge transfer resistance than the (101)-dominated one, supporting

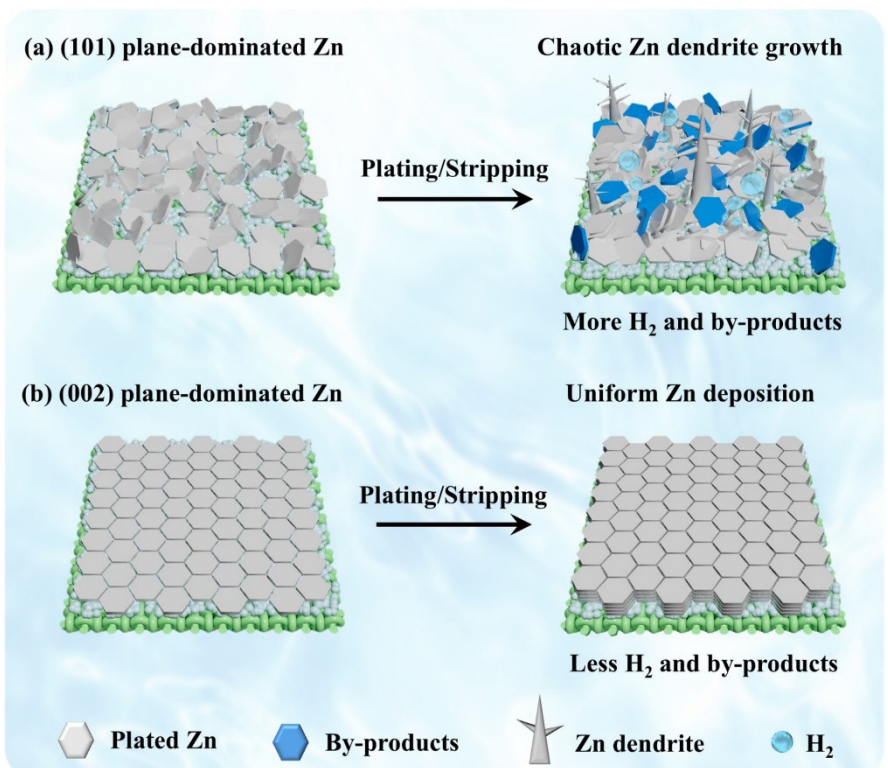


Figure 4. The working mechanism of (101)- (a) and (002)- (b) dominated Zn electrodes.

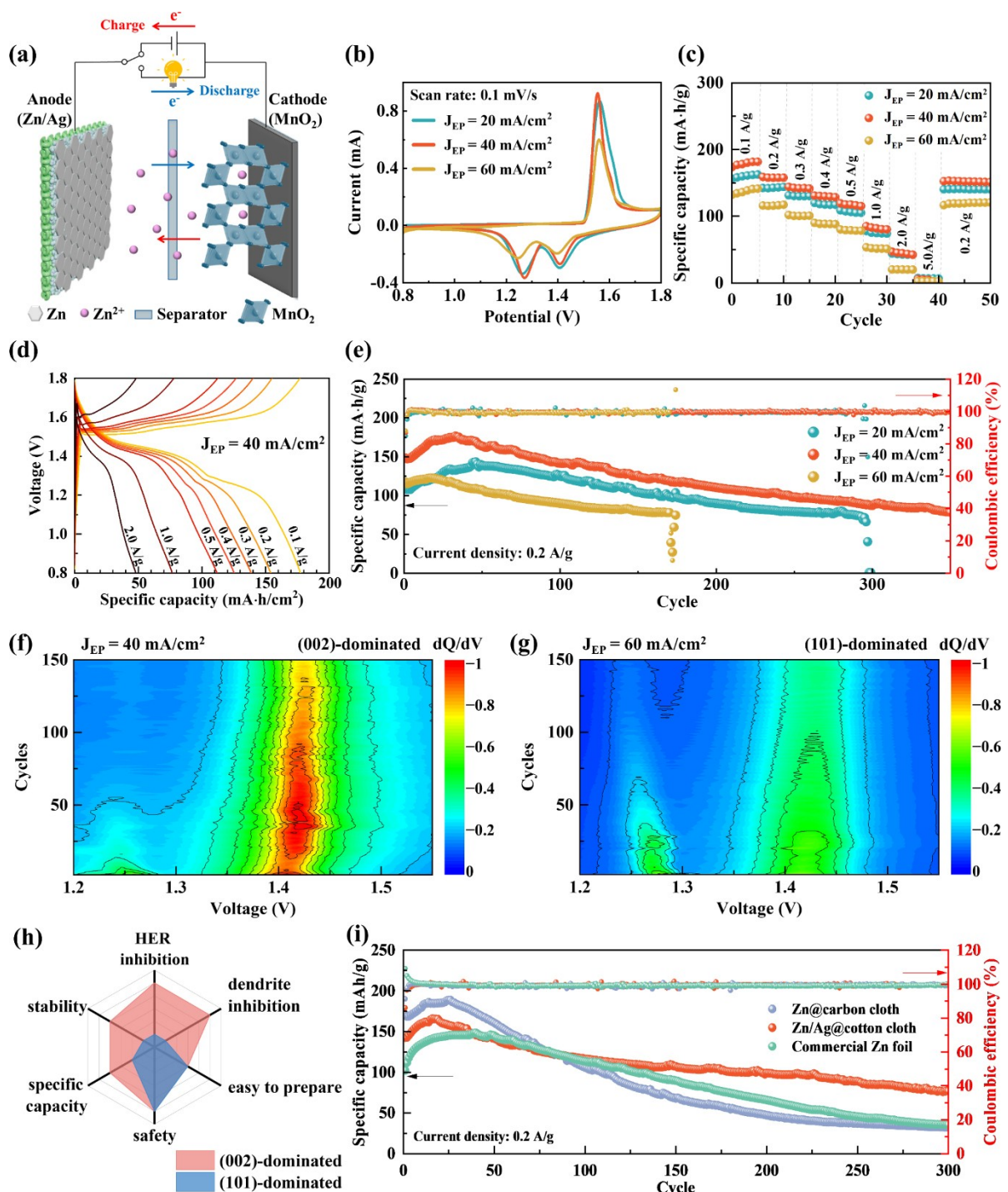


Figure 5. (a) Schematic of a Zn/Ag@cotton cloth||MnO₂ full cell in different operating states. (b) CV curves of full batteries paired with different anodes in the voltage range of 0.8–1.8 V at a scan rate of 0.1 mV/s. (c) Rate performances of full batteries at various current densities. (d) GCD curves of the ZIBs with Zn electroplated at a current density of $J_{EP} = 40 \text{ mA}/\text{cm}^2$. (e) Long-term cyclability of different anodes at a current density of 0.2 A/g. Differential capacity analysis of full batteries using anodes fabricated at electroplating current densities of 40 mA/cm² (f) and 60 mA/cm² (g). (h) A radar chart compares different properties of (002) and (101)-dominated electrodes. (i) The long-term stability of anodes based on different substrates, including Zn@carbon cloth, Zn/Ag@cotton cloth, and commercial Zn foil.

the argument regarding the higher specific capacity of the (002)-oriented electrode.

Figure 5c shows the rate performances of various full batteries over a current density range from 0.1 to 5.0 A/g. The anode prepared under $J_{EP} = 40 \text{ mA}/\text{cm}^2$ exhibits the highest

specific capacity across all current densities, compared to the other two electrodes. When the current density is returned to the initial value of 0.2 A/g, the anode also demonstrates good reversibility at 96.7%. This high reversibility can be attributed to the (002)-dominated electrode's ability to suppress hydrogen

evolution reactions and by-product generation. Figure 5d and Figure S13 show the GCD curves of various full batteries at different current densities. During the charging process, the plateau region occurs at 1.56 V, while the discharging process provides two distinct plateau regions at approximately 1.40 V and 1.23 V. ZIBs with Zn electroplated at $J_{EP}=40\text{ mA/cm}^2$ demonstrate the highest specific capacity.

Figure 5e demonstrates the stability of three types of full batteries at a current density of 0.2 A/g. The full battery with the Zn anode electroplated at a current density of $J_{EP}=40\text{ mA/cm}^2$ delivers the highest specific capacity of 148.3 mA·h/g during the initial cycle, which aligns with the prediction derived from the CV measurements. After operating for 300 cycles, the Zn anode fabricated at $J_{EP}=40\text{ mA/cm}^2$ also shows the best capacity retention, at 58.8%. At another current density of 1 A/g, the full battery paired with the anode electroplated at $J_{EP}=40\text{ mA/cm}^2$ also exhibits the largest initial specific capacity and the best long-term stability (Figure S14). Therefore, compared to the (101)-dominated Zn anode, the (002)-oriented one enhances the specific capacity and stability of the full battery, achieving high-performance Zn-ion batteries.

Figures 5f and 5g compare differential capacity plots (i.e., dQ/dV vs. V) of full batteries with anodes fabricated at current densities of 40 mA/cm^2 and 60 mA/cm^2 respectively. Differential capacity plots are commonly used to characterize the degradation mechanisms of rechargeable batteries by evaluating changes in peak height and position. Figure S15 aligns the coordination of the GCD curve with its differential capacity plot, suggesting that the peaks in the differential capacity plot correspond to the plateaus of the GCD curves. In Figures 5f and 5g, the distinct peaks at approximately 1.44 V and 1.26 V correspond to the insertion of H^+ and Zn^{2+} ions into MnO_2 , respectively. For the peak caused by the insertion of Zn^{2+} ions, the (101)-dominated electrode shows a faster reduction in peak height and a significant shift toward lower voltage compared to the (002)-dominated electrode. This behavior is likely due to the loss of Zn inventory, resulting from the rapid formation of chaotic Zn dendrites on the surface of the (101)-dominated anode. For the peak related to H^+ ion insertion, neither electrode shows a significant peak shift, only a decrease in peak height. This phenomenon suggests the loss of active material, possibly due to the disorder of the MnO_2 crystal structure during cyclic testing. However, the (002)-dominated electrode exhibits much slower degradation than the (101)-dominated one. Therefore, the (002)-dominated electrode achieves higher stability during long-term galvanostatic measurements, as well as better performance in Zn-ion batteries.

Figure 5h summarizes the advantages of the (002)-dominated electrode in Zn-ion battery applications, compared to the (101)-dominated one. The (002)-dominated electrode enables better HER suppression and dendrite inhibition, resulting in higher long-term stability and specific capacity. Both electrodes are immersed in the aqueous electrolyte, preventing the rapid spontaneous combustion of cotton cloth at high temperatures, ensuring high safety for both electrodes. Compared to other electrodes (e.g., commercial Zn foil), these electrodes require a slightly more complex fabrication process. To further demon-

strate the potential of (002)-dominated Zn anodes in practical scenarios, we assembled small pouch cells ($2\times 3\text{ cm}^2$), which maintain good retention of specific capacity after operation at a current density of 0.2 A/g (see Figure S16). Additionally, the pouch cell demonstrates exceptional flexibility, maintaining stable open-circuit voltage even under extreme bending conditions, up to 180° (see Figure S17). This good mechanical flexibility indicates the promising potential for integration with wearable electronic devices, further broadening the application range of aqueous Zn-ion batteries, as illustrated in Figure S18.

Figure 5i demonstrates the cyclic stability of full batteries with different anodes prepared on various substrates. In addition to commercial Zn foils, we also electroplated a (002)-dominated Zn layer onto a conductive cloth substrate, referred to as Zn@carbon cloth. Since the commercial Zn foil is (101)-dominated, it is expected to show lower specific capacity in the initial cycle and poorer stability than our anode. Interestingly, the Zn@carbon cloth anode also exhibits lower stability than our anode, despite having a higher initial specific capacity. This is because both carbon cloth and cotton cloth exhibit a high specific surface area, as shown in Figures S19a–S19d. However, cotton cloth was coated with Ag powder mixed with a binder to prepare a conductive cloth, which reduced its specific surface area (Figure S19f–S19 g). When Zn was electroplated onto both conductive cloths, Zn nucleated and grew in various planes and directions, depending on the surface texture of the cloth (Figures S20b and S20c). During cyclic testing, Zn@carbon cloth initially provided higher specific capacity than Zn@Ag@cotton cloth due to its larger specific area, resulting in a larger interaction region during the charge/discharge process. However, the non-uniform Zn growth on the fiber surface of Zn@carbon cloth, caused by electroplating in various directions, led to a decrease in specific capacity over subsequent cycles. The enhanced stability of our anode may be attributed to the addition of the silver conductive layer, warranting further investigation into its contribution in future studies.

3. Conclusions

In summary, we have demonstrated a novel substrate composed of a silver conductive layer and a cotton supporting layer for electroplating (002)-dominated Zn anodes. Based on the analysis of nucleation and crystal growth, both the electroplating current density and time are found to play critical roles in forming a dense and flat (002)-dominated Zn layer. The optimal conditions for achieving this include an electroplating current density of $J_{EP}=40\text{ mA/cm}^2$ and an electroplating time of 30 minutes. Compared to the (101)-dominated anode, the (002)-dominated electrode exhibits several advantages in battery applications, including faster Zn deposition kinetics, lower charge transfer resistance, and reduced H_2 and by-product generation, all of which enable better suppression of dendrite growth and enhanced Zn-ion battery performance. Furthermore, the (002)-dominated Zn layer atop our modified cotton substrate exhibits higher specific capacity and better stability than the Zn layer on carbon cloth, highlighting the

advantages of the novel substrate in Zn-ion battery applications. The good flexibility of the electroplated (002)-dominated layer on modified cotton cloth opens up promising possibilities for integrating Zn-ion batteries as a power source in wearable devices.

Experimental Section

Materials

Ag powders with a particle size of 1~3 μm were purchased from Shanghai Jinzhuan Alloy Co., Ltd. Sodium hydroxide (NaOH), zinc sulfate heptahydrate ($\text{ZnSO}_4 \cdot 7\text{H}_2\text{O}$), sodium sulfate (Na_2SO_4), sodium chloride (NaCl), boric acid (H_3BO_3), and N,N-Dimethylformamide (DMF) were purchased from CARLO ERBA. Commercial manganese dioxide (MnO_2), polyvinylidene fluoride (PVDF), and conductive carbon (acetylene black) powder were purchased from Wuxi Admas Technology.

Preparation of the Modified Cotton Cloth

The commercial cotton cloth, with dimensions of $11 \times 21 \text{ cm}^2$, was immersed in 1 M NaOH at 85~90°C for 1 hour. Then, the cotton cloth was rinsed several times with deionized water and dried in an oven overnight. Next, 48 g of Ag powder was mixed with 6 g of ethyl methacrylate copolymer dissolved in 120 mL of acetone to prepare the Ag paint. The cleaned cloth was coated with the Ag paint to a thickness of 60 μm using a doctor blade and dried at ambient temperature for 15 minutes. The process was repeated on the other side of the cloth to fabricate the electrically conductive cotton cloth, referred to as Ag cloth. We chose a thickness of 60 μm to coat Ag on the cotton cloth because it is the minimum thickness that can cover the entire surface of the cloth (Figures S21). The battery performance of symmetric cells and $\text{Zn}||\text{MnO}_2$ full-cell batteries with varying Ag layer thicknesses of 30 and 60 μm is shown in Figure S22. The results obtained with the 60 μm thickness demonstrate better stability in symmetric batteries, as well as better rate performance and long-term stability at 1.0 A/g for $\text{Zn}||\text{MnO}_2$ full batteries.

Preparation of the Zn–Ag/Cotton Cloth Electrode

100 g of $\text{ZnSO}_4 \cdot 7\text{H}_2\text{O}$, as the Zn source, 40 g of Na_2SO_4 as the supporting electrolyte, 20 g of NaCl for conductivity improvement, and 8 g of H_3BO_3 as a pH buffer were dissolved in 500 mL of deionized water to prepare the Zn electrolyte solution. During the Zn electroplating process, Pt mesh and Ag cloth were employed as anodes and cathodes, respectively. Zn was electroplated onto one side of the Ag cloth at varying current densities, maintaining a constant areal capacity of 20 $\text{mA} \cdot \text{h}/\text{cm}^2$. The electroplated area was $3.5 \times 3.5 \text{ cm}^2$.

Material Characterizations

The microstructures of the electroplated Zn on the conductive cotton cloth were characterized using scanning electron microscopy (SEM, Hitachi SU3500). Phase identification and structural orientation were conducted via standalone X-ray diffraction (XRD, Rigaku RINT2100) with a Cu $\text{K}\alpha$ X-ray source. The surface roughness of the electroplated Zn at different current densities was measured using a confocal laser scanning microscope (CSLM, Olympus LEXT OLS500) with a laser wavelength of 405 nm. Grazing incidence X-ray diffraction (GIXRD) with a synchrotron light source (1.2 GeV) at

BL1.1 W: Multiple X-ray Techniques (MXT), Synchrotron Light Research Institute (SLRI), Nakhon Ratchasima, Thailand, was also employed.

Electrochemical Tests

The active material, commercial MnO_2 powder, was ball-milled for 300 minutes with ethanol and then dried in an oven at 75°C for 24 hours. The active material, conductive carbon, and PVDF dissolved in DMF were mixed in a mass ratio of 7:2:1 until it became a homogeneous slurry. The slurry was coated onto graphite paper using a doctor blade with a thickness of 120 μm , and then dried in a vacuum oven at 80°C. Coin cells (CR2032) were used to assemble full cells ($\text{Zn}||\text{MnO}_2$) and symmetric cells ($\text{Zn}||\text{Zn}$). Glass fiber (GF/C) and 2 M ZnSO_4 were used as separators and electrolytes, respectively. Galvanostatic charge/discharge tests were performed using a NEWARE battery tester. Cyclic voltammetry (CV) of full cells was conducted with a scan rate of 0.1 mV/s within a voltage range of 0.8~1.8 V. Electrochemical impedance spectroscopy (EIS) was measured in a frequency range from 1×10^{-2} to 1×10^5 Hz using an electrochemical workstation (CHI660e).

Author Contributions

N.K. and C.T. conducted the fabrication and measurements. N.K. and Z.S. analyzed data. S.W. and X.Z. performed the calculations and in situ XRD experiment and data analysis, P.W. and J.Q. conceived the project and contributed to the experimental design. All authors analyzed the results, wrote and revised the manuscript and agreed on the manuscript.

Acknowledgements

This research has received funding support from the Thailand Science Research and Innovation Fund Chulalongkorn University and National Research Council of Thailand (NRCT) (N11A670659). The Scholarship from the Graduate School, Chulalongkorn University to commemorate the 72nd anniversary of His Majesty King Bhumibol Adulyadej is gratefully acknowledged.

Conflict of Interests

The authors declare no conflict of interest.

Data Availability Statement

The data that support the findings of this study are available from the corresponding author upon reasonable request.

Keywords: (002)-oriented Zn textures • Cotton cloth • Electroplating • Stability • Zn-ion batteries

- [1] a) C. Li, X. Xie, S. Liang, J. Zhou, *Energy Environ. Mater.* **2020**, *3*, 146; b) X. Jia, C. Liu, Z. G. Neale, J. Yang, G. Cao, *Chem. Rev.* **2020**, *120*, 7795; c) H. He, H. Qin, J. Wu, X. Chen, R. Huang, F. Shen, Z. Wu, G. Chen, S. Yin, J. Liu, *Energy Storage Mater.* **2021**, *43*, 317.
- [2] a) J. Yang, B. Yin, Y. Sun, H. Pan, W. Sun, B. Jia, S. Zhang, T. Ma, *Nano-Micro Lett.* **2022**, *14*, 42; b) T. Zhang, Y. Tang, S. Guo, X. Cao, A. Pan, G. Fang, J. Zhou, S. Liang, *Energy Environ. Sci.* **2020**, *13*, 4625; c) N. Wang, H. Wan, J. Duan, X. Wang, L. Tao, J. Zhang, H. Wang, *Mater. Today Adv.* **2021**, *11*, 100149; d) S. Chen, H. Wang, M. Zhu, F. You, W. Lin, D. Chan, W. Lin, P. Li, Y. Tang, Y. Zhang, *Nanoscale Horiz.* **2023**, *8*, 29.
- [3] a) J. Abdulla, J. Cao, P. Wangyao, J. Qin, *J. Met. Mater. Miner.* **2020**, *30*, 1; b) Z. Li, T. T. Beyene, K. Zhu, D. Cao, *J. Met. Mater. Miner.* **2024**, *34*, 2009.
- [4] a) C. Nie, G. Wang, D. Wang, M. Wang, X. Gao, Z. Bai, N. Wang, J. Yang, Z. Xing, S. Dou, *Adv. Energy Mater.* **2023**, *13*, 2300606; b) Y. Gong, B. Wang, H. Ren, D. Li, D. Wang, H. Liu, S. Dou, *Nano-Micro Lett.* **2023**, *15*, 208; c) S. Mallick, C. R. Raj, *ChemSusChem* **2021**, *14*, 1987.
- [5] a) Y. Zhang, X. Zheng, N. Wang, W.-H. Lai, Y. Liu, S.-L. Chou, H.-K. Liu, S.-X. Dou, Y.-X. Wang, *Chem. Sci.* **2022**, *13*, 14246; b) M. Liu, W. Yuan, X. Qu, X. Ru, X. Li, T. Wang, X. Wang, Y. Wang, Y. Liu, N. Zhang, *Energy Environ. Sci.* **2024**, *17*, 9611.
- [6] a) X. Yin, J. Feng, Y. Chen, J. Zhang, F. Wu, W. Liu, W. Shi, X. Cao, *J. Solid State Electrochem.* **2023**, *27*, 1329; b) J. Chen, M. Chen, H. Ma, W. Zhou, X. Xu, *Energy Reviews* **2022**, *1*, 100005.
- [7] a) L.-F. Zhou, T. Du, J.-Y. Li, Y.-S. Wang, H. Gong, Q.-R. Yang, H. Chen, W.-B. Luo, J.-Z. Wang, *Mater. Horiz.* **2022**, *9*, 2722; b) Y. Liang, M. Qiu, P. Sun, W. Mai, *Adv. Funct. Mater.* **2023**, *33*, 2304878; c) C. Liu, X. Xie, B. Lu, J. Zhou, S. Liang, *ACS Energy Lett.* **2021**, *6*, 1015.
- [8] a) V. Jabbari, T. Foroozan, R. Shahbazian-Yassar, *Adv. Energy Sustainability Res.* **2021**, *2*, 2000082; b) T. Wang, J. Sun, Y. Hua, B. N. V. Krishna, Q. Xi, W. Ai, J. S. Yu, *Energy Storage Mater.* **2022**, *53*, 273; c) S. Wu, Z. Hu, P. He, L. Ren, J. Huang, J. Luo, *eScience* **2023**, *3*, 100120; d) W. Yuan, X. Nie, G. Ma, M. Liu, Y. Wang, S. Shen, N. Zhang, *Angew. Chem. Int. Ed.* **2023**, *62*, e202218386; e) J. Zhang, W. Huang, L. Li, C. Chang, K. Yang, L. Gao, X. Pu, *Adv. Mater.* **2023**, *35*, 2300073; f) G. Ma, W. Yuan, X. Li, T. Bi, L. Niu, Y. Wang, M. Liu, Y. Wang, Z. Shen, N. Zhang, *Adv. Mater.* **2024**, *36*, 2408287.
- [9] X. Zhang, J. Li, Y. Liu, B. Lu, S. Liang, J. Zhou, *Nat. Commun.* **2024**, *15*, 2735.
- [10] J. Friedrich, *Encyclopedia of Condensed Matter Physics (Second Edition)*, (Ed: T. Chakraborty), Academic Press, Oxford 2024, p. 190.
- [11] P. S. Dutta, *Comprehensive Semiconductor Science and Technology* (Eds: P. Bhattacharya, R. Fornari, H. Kamimura), Elsevier, Amsterdam 2011, p. 36.
- [12] Y. D. Gamburg, G. Zangari, *Theory and Practice of Metal Electrodeposition* Springer New York, New York, NY 2011, p.1.
- [13] Q. Ren, X. Tang, X. Zhao, Y. Wang, C. Li, S. Wang, Y. Yuan, *Nano Energy* **2023**, *109*, 108306.
- [14] S.-B. Wang, Q. Ran, R.-Q. Yao, H. Shi, Z. Wen, M. Zhao, X.-Y. Lang, Q. Jiang, *Nat. Commun.* **2020**, *11*, 1634.
- [15] Y. Yan, C. Shu, T. Zeng, X. Wen, S. Liu, D. Deng, Y. Zeng, *ACS Nano* **2022**, *16*, 9150.
- [16] A. S. Khanna, *Handbook of Environmental Degradation of Materials (Second Edition)* (Ed: M. Kutz), William Andrew Publishing, Oxford 2012, p. 127.
- [17] J. Ji, Z. Zhu, H. Du, X. Qi, J. Yao, H. Wan, H. Wang, L. Qie, Y. Huang, *Adv. Mater.* **2023**, *35*, 2211961.
- [18] D. Wang, J. Sun, Q. Xue, Q. Li, Y. Guo, Y. Zhao, Z. Chen, Z. Huang, Q. Yang, G. Liang, B. Dong, C. Zhi, *Energy Storage Mater.* **2021**, *36*, 272.
- [19] J. Zheng, X. Liu, Y. Zheng, A. N. Gandi, X. Kuai, Z. Wang, Y. Zhu, Z. Zhuang, H. Liang, *Nano Lett.* **2023**, *23*, 6156.
- [20] X. Xiao, E. Liu, J. Shao, S. Ge, *J. Appl. Biomater. Funct. Mater.* **2021**, *19*, 228000211062407.
- [21] G. D. Wilcox, D. R. Gabe, *Transactions of the IMF* **1992**, *70*, 93.
- [22] H. Lu, Q. Jin, X. Jiang, Z.-M. Dang, D. Zhang, Y. Jin, *Small* **2022**, *18*, 2200131.
- [23] Z. Hou, Y. Gao, R. Zhou, B. Zhang, *Adv. Funct. Mater.* **2022**, *32*, 2107584.
- [24] S. D. Pu, C. Gong, Y. T. Tang, Z. Ning, J. Liu, S. Zhang, Y. Yuan, D. Melvin, S. Yang, L. Pi, J.-J. Marie, B. Hu, M. Jenkins, Z. Li, B. Liu, S. C. E. Tsang, T. J. Marrow, R. C. Reed, X. Gao, P. G. Bruce, A. W. Robertson, *Adv. Mater.* **2022**, *34*, 2202552.
- [25] a) M. Zhou, S. Guo, J. Li, X. Luo, Z. Liu, T. Zhang, X. Cao, M. Long, B. Lu, A. Pan, G. Fang, J. Zhou, S. Liang, *Adv. Mater.* **2021**, *33*, 2100187; b) X. Liu, Y. Guo, F. Ning, Y. Liu, S. Shi, Q. Li, J. Zhang, S. Lu, J. Yi, *Nano-Micro Lett.* **2024**, *16*, 111.
- [26] J. Zhang, J. Sun, D. Yang, S. Ha, T. Ma, H. Liu, X. Shi, D. Guo, Y. Wang, Y. Wei, *Nano Lett.* **2024**, *24*, 688.
- [27] a) Z. You, W. Hua, N. Li, H. Liu, J.-G. Wang, *Chin. Chem. Lett.* **2023**, *34*, 107525; b) M. Chamoun, W. R. Brant, C.-W. Tai, G. Karlsson, D. Noréus, *Energy Storage Mater.* **2018**, *15*, 351.

Manuscript received: November 12, 2024

Revised manuscript received: January 19, 2025

Accepted manuscript online: January 26, 2025

Version of record online: February 7, 2025